DISCLAIMER

This report was prepared as an account of work sponsored by an agency of the United States Government. Neither the United States Government nor any agency thereof, nor any of their employees, makes any warranty, express or implied, or assumes any legal liability or responsibility for the accuracy, completeness, or usefulness of any information, apparatus, product, or process disclosed, or represents that its use would not infringe privately owned rights. Reference herein to any specific commercial product, process, or service by trade name, trademark, manufacturer, or otherwise does not necessarily constitute or imply its endorsement, recommendation, or favoring by the United States Government or any agency thereof. The views and opinions of authors expressed herein do not necessarily state or reflect those of the United States Government or any agency thereof. Reference herein to any social initiative (including but not limited to Diversity, Equity, and Inclusion (DEI); Community Benefits Plans (CBP); Justice 40; etc.) is made by the Author independent of any current requirement by the United States Government and does not constitute or imply endorsement, recommendation, or support by the United States Government or any agency thereof.

LLNL-SR-2002916

Microstructurally-Inspired Strategies to Print Tantalum and Tantalum-Tungsten Alloys

A. Lew, W. Cai, P. DePond, S. Park

December 2024

Microstructurally-Inspired Strategies to Print Tantalum and Tantalum-Tungsten Alloys

Adrian J. Lew, Wei Cai, Phil Depond, Seongyun Park

Mechanical Engineering
Stanford University

Prepared by LLNL under Contract DE-AC52-07NA27344.

1 Introduction

1.1 Motivation

The goal of this project is to investigate strategies to print tantalum and tantalum- tungsten alloys, which are notoriously difficult to print with consistent results because of the sensitivity of the properties to small concentrations of interstitial impurities (particularly oxygen) and microstructure, and hence to processing conditions. The ultimate tensile stress (UTS) for non-additively manufactured Ta as a function of temperature shows a stunning variation [2,3]. In direct metal laser sintering (DMLS) Ta, a strong dependence of porosity, grain morphology and texture on processing conditions was found [1].

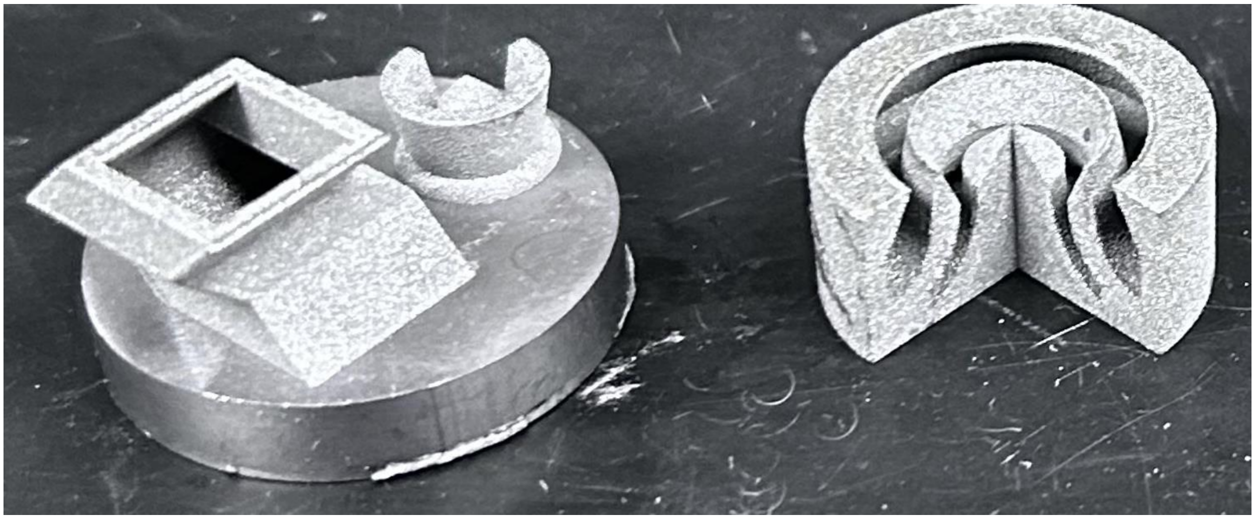

Figure 1.1: Examples of complex geometries printed in Ta-10W. On the left, a complex prismatic tube, and on the right, a complex curved cavity which was purposedly printed with a missing quadrant to display its interior surfaces. None of these geometries can be made through milling, and casting would be highly complex. Notice that low angle planes were printed without supports; this is crucial since removing support structures from internal cavities would be a very complex task.

A similar behavior is observed in pure tungsten, in which the UTS can vary from 1432 MPa in the stress-relieved condition to 38 MPa in the recrystallized condition [4]. Additionally, Ta-W alloys with > 90% tungsten are prone to fracture while printed. These difficulties to print majority-tungsten alloys parallels the known difficulties to form it, as illustrated in Fig. 1.1(right). The wide, microstructurally-dependent range of the UTS makes it impossibly challenging to find the printing conditions to minimize crack appearance in tungsten printing.

Finally, it does not help that tungsten and tantalum are the elements with the first and fourth highest melting temperature, respectively. While printed, the material undergoes large thermal cycles and thermal expansion, and depending on how this cycling is performed, extensive recrystallization. It is precisely the dependence of the recrystallization temperature on the presence of impurities that has been argued as responsible for the observed range of mechanical behavior.

Tantalum-tungsten alloys are traditionally made with 2.5%-10% tungsten in order to strengthen Tantalum while retaining its ability to be formed. However, additive manufacturing of Ta-W alloys opens the possibility of obtaining net shape parts, and hence the ability to take advantage of further strengthening that may result of higher tungsten mass fractions.

With this context in mind, the goals of this project are:

- Determine if it is possible to obtain homogeneous alloys by mixing W and Ta powders after printing, or in-situ alloying.
- A method to print Ta-W cubes with consistent mechanical properties and characteristic microstructure, with 2.5% and 10% tungsten content.
- Evaluate the effect of oxygen content in printing tungsten.
- Demonstrate the printing of complex geometries with Ta-W alloys, and characterization of metallurgical and mechanical properties of such parts.

If the project is successful, there will be a method to print complex geometries with Ta, Ta2.5W, Ta5W, and Ta10W with consistent microstructure.

1.2. Timeline for Key Deliverables and Milestones

	Q1-2023	Q2-2023	Q3-2023	Q4-2023	Q1-2024	Q2-2024	Q3-2024
Proven method to mix Ta-W powders	🟦	🟦					
Proven method to print Ta-W cubes	🟥	🟥	🟥				
Show the effect of oxygen depletion on tungsten prints	🟩	🟩	🟩	🟩			
Print Ta-W inclined planes without support.	🟧	🟧	🟧	🟧	🟧	🟧	
Print complex geometries with Ta-W.	🟪	🟪	🟪	🟪	🟪	🟪	🟪

Figure 1.2. Gantt chart of the project

Monthly updates and quarterly presentations have been provided.

1.3 FY23-24 Accomplishments

In FY23-24, we made progress in following area:

- We showed that by depleting oxygen in tungsten powder we observe a noticeable decrease in the density of cracks in printed tungsten.
- We developed strategies to print inclined planes that form angles above 10° with the horizontal without support with Ta-10W. We did not try to print under 10° yet, and only started to adapt the strategy to other alloy grades.
- We used the strategy developed to print inclined planes to create a way to print complex geometries, such as those shown in Fig. 1.1.

2 In Situ Alloying Ta and W

We successfully developed a method to perform in situ alloying of Ta and W in LPBF machines.

2.1 Experimental/modeling approaches- including supplier information

The commercial Ta and W spherical powders (Stanford Advanced Materials, CA, USA), both with purities over 99.9 % and with 15 – 53 μm in diameter, were used to print pure Ta, Ta-2.5W, and Ta-10W alloys, respectively. To create the Ta-2.5W and Ta-10W alloys, W powders were mixed with Ta powders in weight ratios of 2.5:97.5 and 1:9, respectively. These were mechanically blended using a commercial powder mixer (MSK-SFM-TR-2K, MTI, USA) at 70 revolutions-per-minute for 12 hours. The blended powders were then sieved to minimize agglomerations before being loaded into a LPBF machine (TruPrint 1000, TRUMPF, USA). These powders were then used to print cubes, as detailed in part 4.

2.2 Results/Outcomes

The representative photographic image for Ta-10W powders after blending and sieving is shown in Fig. 2.1 (a). The spherical shapes without significant changes or agglomerations are still maintained on the mixed powders. Fig. 2.1 (b) shows XRD results for Ta-10W mixed powders (black solid line) and the printed parts of Ta (blue solid line), Ta-2.5W (brown solid line), and Ta-10W (yellow solid line), respectively. The XRD peaks for the Ta-10W powder are related to pure Ta and W with body-center cubic (BCC) single phases, respectively. In contrast, in the XRD result for the pure Ta printed part, the W peak disappears and only Ta peaks are observed. The Ta-2.5W and Ta-10W printed parts, similar to pure Ta, do not show W peaks and only show Ta-related peaks, which are slightly shifted to the right compared to the pure Ta peaks. The extent of the shift increases with higher W content, i.e., in the order of Ta-10W, Ta-2.5W, and Ta, which is attributed to a substitutional solid solution of W into Ta matrix. For the XRD results of the Ta-10W powder, the 2-theta angles for the Ta and W in the region marked with a black dashed box were 69.2° and 73.2°, respectively. Using Vegard's law to calculate the 2-theta value for Ta-10W yielded a value of 70.0°. This value is almost identical to the XRD value experimentally measured for the Ta-10W part, which is 69.9°.

Fig. 2.1 (c) and (d) shows the SEM-EDS spectral imaging results for the Ta-10W printed part. Distributions of the Ta and W elements are relatively uniform across a large area. Table 2.1 presents the results of the compositional analysis performed using SEM-EDS on the printed parts of Ta, Ta-2.5W, and Ta-10W, respectively. Each result represents the average of measurements taken from ten points on each part. The contents of W in the printed Ta-2.5W and Ta-10W alloys are 2.58 ± 0.19 %, 10.4 ± 0.41 %, respectively. There is no significant difference between the W content in the final printed Ta-W alloys and the pre-designed 2.5 % and 10% W-mixed powders. These results indicate that the un-alloyed powders used in this study were successfully in-situ alloyed into the intended compositions during the LPBF process.

	Ta	Ta-2.5W	Ta-10W
Ta	100	97.44 ± 0.22	89.67 ± 0.44
W	0	2.58 ± 0.19	10.4 ± 0.41

Table 2.1. Compositions of each Ta, Ta-2.5W, and Ta-10W parts measured from EDS results, respectively (averaging ten sampling points).

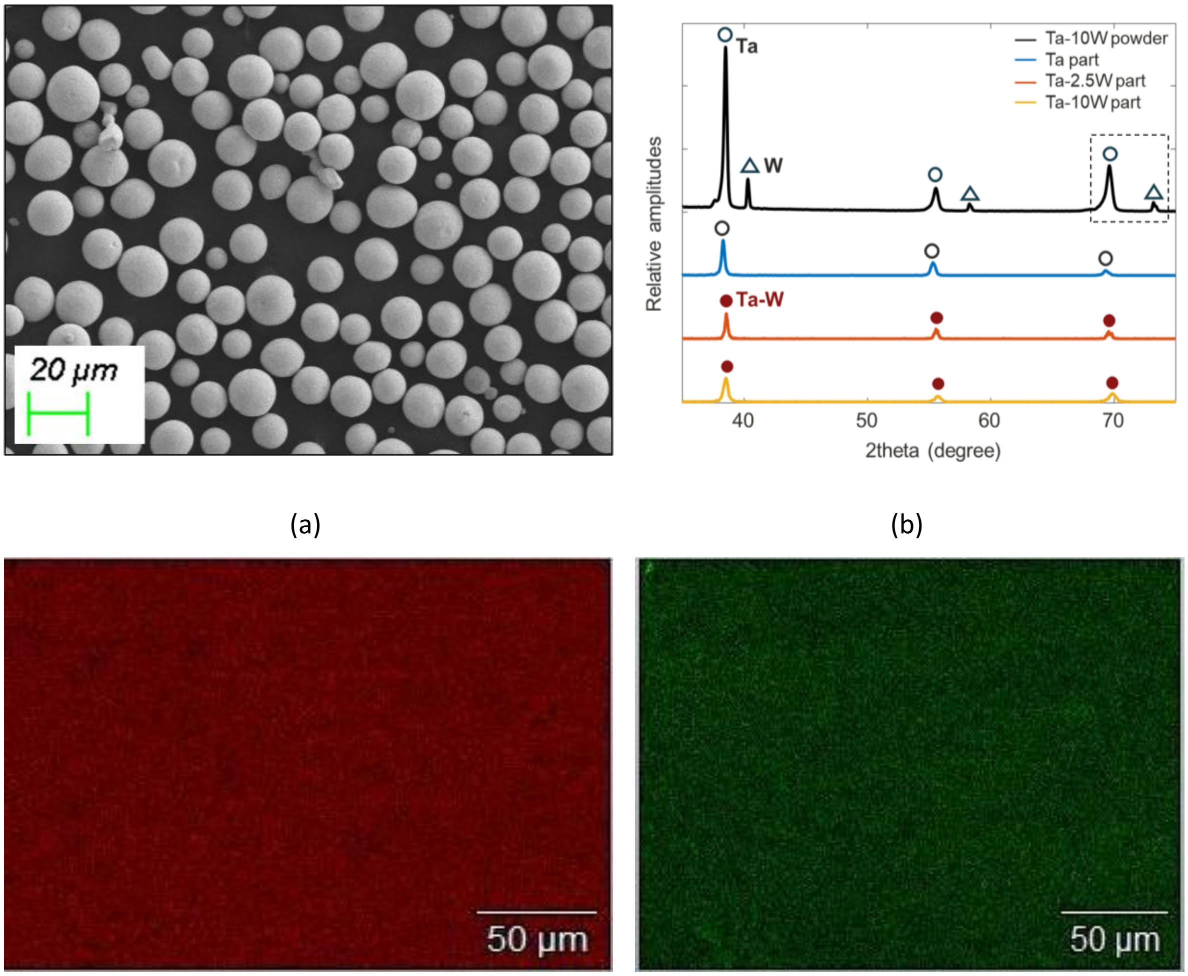

(a)

(b)

(c)

(d)

Figure 2.1. (a) A Ta-10W powder after mixing and sieving. (b) a XRD result for the Ta-10W powder, and the Ta, Ta-2.5W, and Ta-10W printed parts, respectively. EDS images for the Ta-10W parts: (c) Ta and (d) W maps.

3 **Printing with Oxygen-Depleted Tungsten**

3.1 Experimental/modeling approaches

Tungsten W45 and W25 powders (Tekna, Canada) were used for all single track and full build experiments. Single powder layer, single track experiments were performed to understand the laser melting at the scan vector level. Optical and electron microscopy was performed to measure the dimensions of the resolidified melt pools to plan full build experiments.

A Trumpf Truprint 1000 LPBF system (Fig. 3.1) was used for all laser melting experiments. It is designed for production environments needing high build rates and consistent quality. It has an attached glovebox for inert powder handling with sensitive materials. It has a build envelope of 100 Ø x 120 mm and an ultra small spot size of 30 um with a wavelength of 1070 nm. The machine offers high resolution, (no limit on layer thickness but with an average for 20 um) and high scanning speeds of up to 3 m/s.

Single powder layer, single track experiments were performed to determine the solidified melt pool geometry for full 3D builds. Metallographic analysis was performed on the prepared cross sections and full 3D print parameters were determined from the resulting geometries.

Reduction of Tungsten Oxide from W45 and W25 powders was performed in an isolated ball mill (Fig. 1) that can reach ~600 C temperatures in a reducing atmosphere of hydrogen. Typical hydrogen concentrations were 4-10%H2 bal. Ar/N2. The rate of reduction that occurs with tungsten oxide is seen in Fig. 2. At 550 C, in dry H2, the total reduction of tungsten oxide occurs in around 2 hours. The isolated ball mill was sealed after reduction experiments, and transferred to the Trumpf Truprint 1000 LPBF system for printing experiments. The glovebox was utilized to manipulate the transfer container and prepare the printer under inert conditions.

X-ray photoelectron spectroscopy (XPS) was performed to determine the efficacy of reduction experiments on the resulting powders.

Characterization of the 3D builds was examined with optical and electron microscopy. After extensive polishing and etching procedures, scanning electron microscopy (SEM) revealed the most accuracte contrast of the surface and present defects.

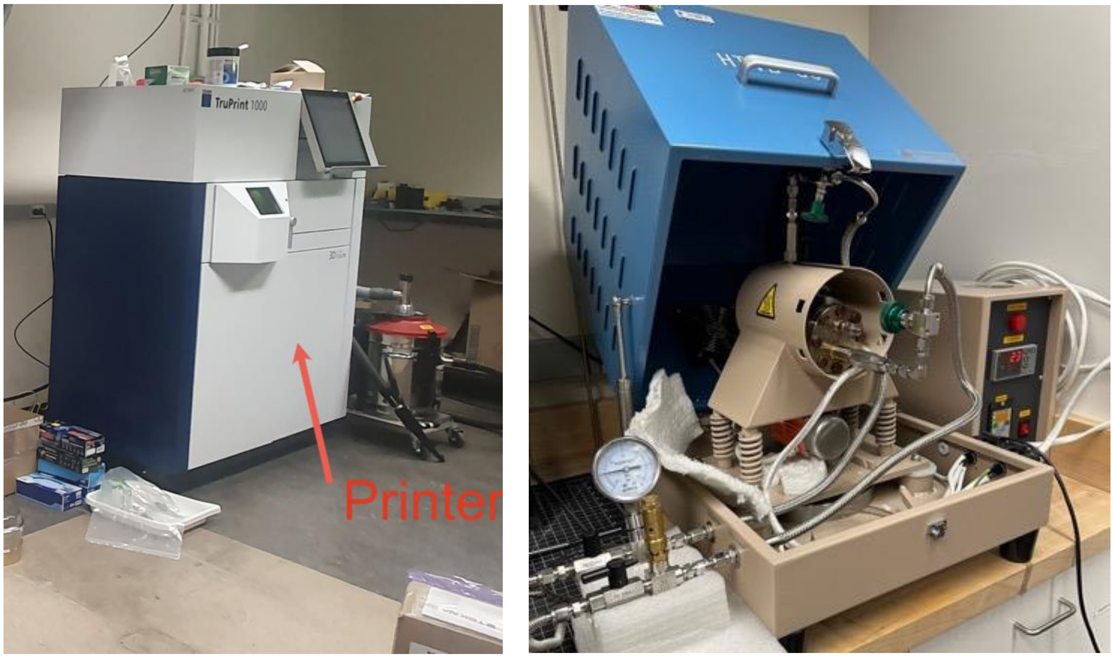

Figure 3.1. (Left) Trumpf 1000 LPBF System. (Right) High temperature ball mill for reducing tungsten oxide in W45/ W25 powders.

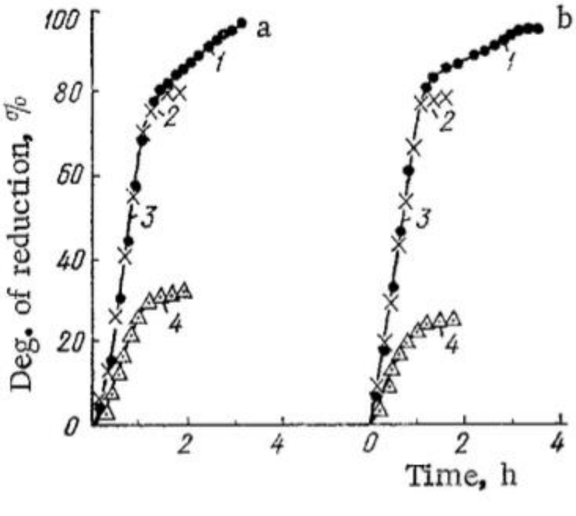

Figure 3.2. Kinetic curves of reduction of tungsten oxide at 550 C. Reproduced from [5].

3.2 Results/Outcomes

Key results from the single track experiments, Table 1, are presented. The melt pool depths and widths are measured, and the maximum hatch spacing for 3D builds is determined using previously determined criterion [6].

width (µm)	depth (µm)	P (W)	V (mm/s)	D/W	D/t (t=20 µm)	Adhesion	Keyhole Transition	hmax (µm)
115.2	58.8	200	100	0.510	2.352	Pass	Pass	96.49
88	28.7	200	200	0.326	1.148	Pass	Pass	64.33
68.6	30.8	200	300	0.448	1.232	Pass	Pass	50.96
94	49	175	200	0.521	1.96	Pass	Pass	76.49
80	29.7	175	300	0.371	1.188	Pass	Pass	58.94

Table 3.1. Melt pool dimensions of select single powder layer, single track experiments. The maximum hatch spacing results from the melt pool dimensions, including acceptability criterion of stable melting regimes.

From the determined conditions in Table 3.1, full build geometries and conditions were applied. An example SEM image of the single-track analysis is shown in Fig. 3.3. The tungsten single tracks were challenging to measure since the grain growth is often epitaxial and could have relatively little texture. Fig. 3.4 shows the layout of test specimens and table of corresponding parameters. The cubes (B) exist as density coupons, and the plates (P) exist as scan strategy coupons to observe the effect of long vs short scan vectors. The resulting 3D build, Figure 3.5, is an example of a printed part that would be further characterized to understand the role of process parameters, and influence of oxygen on part quality.

XPS results of the W45 powder under various reduction conditions corroborates previous studies in which the oxide of tungsten is removed with hydrogen under high heat. While quantitatively measuring the oxygen content is quite challenging, XPS shows a significant change in electron orbital signal from WO3 from the control to the reduced oxgen powder. Figure 3.6 shows the reduction of counts for certain binding energies associated with WO3 of the reduced oxygen powder compared to control.

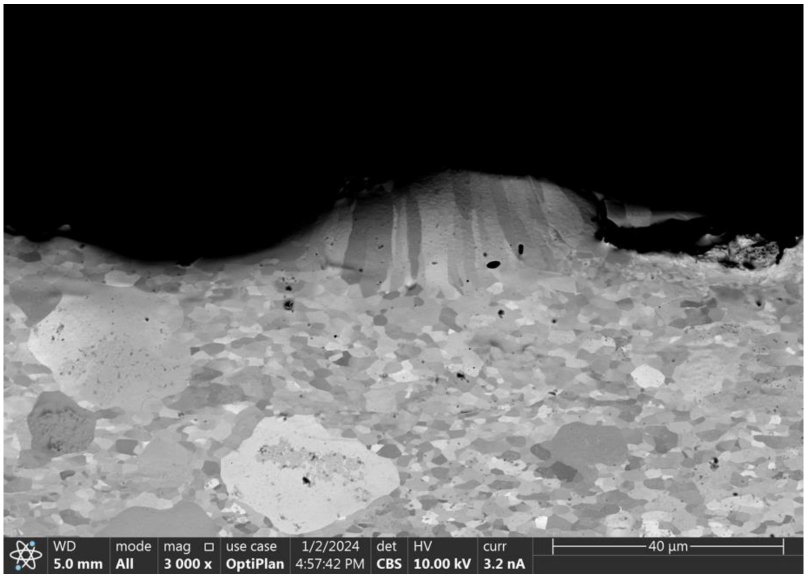

Figure 3.3. Example SEM image of W45 single powder layer, single track melt pool.

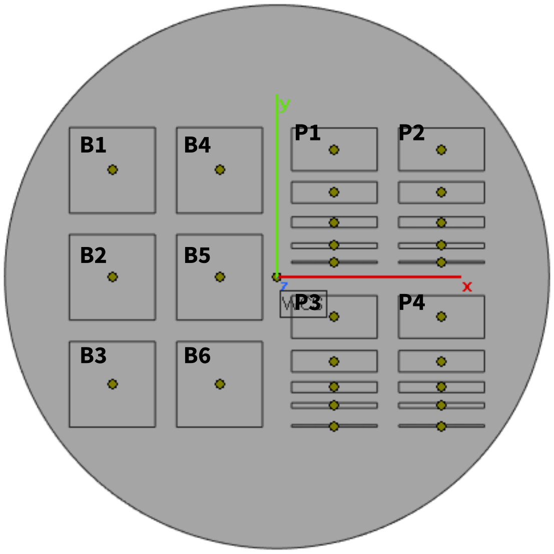

Control Print	P (W)	V (mm/s)	h (um)	Rot (deg.)
B1	200	100	90	90
B2	200	200	65	90
B3	200	300	50	90
B4	175	100	90	90
B5	175	200	65	90
B6	175	300	50	90
P1	200	100	90	0, short
P2	200	100	90	0, short
P3	200	300	50	0, long
P4	200	300	50	0, long

Figure 3.4. Left: Schematic layout of build plate. Right: Parameters associated with schematic parts.

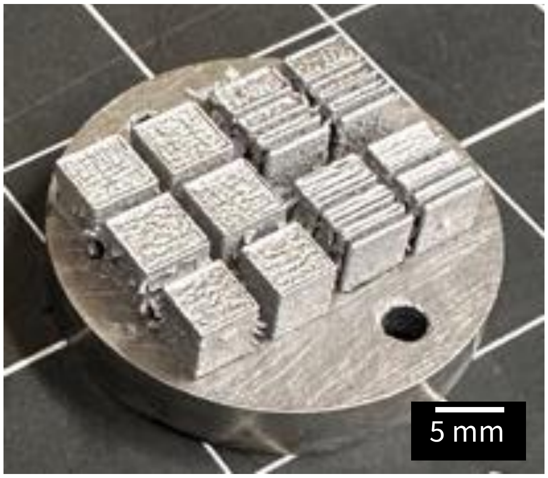

Figure 3.5. Example control print of W45 based on determined process conditions.

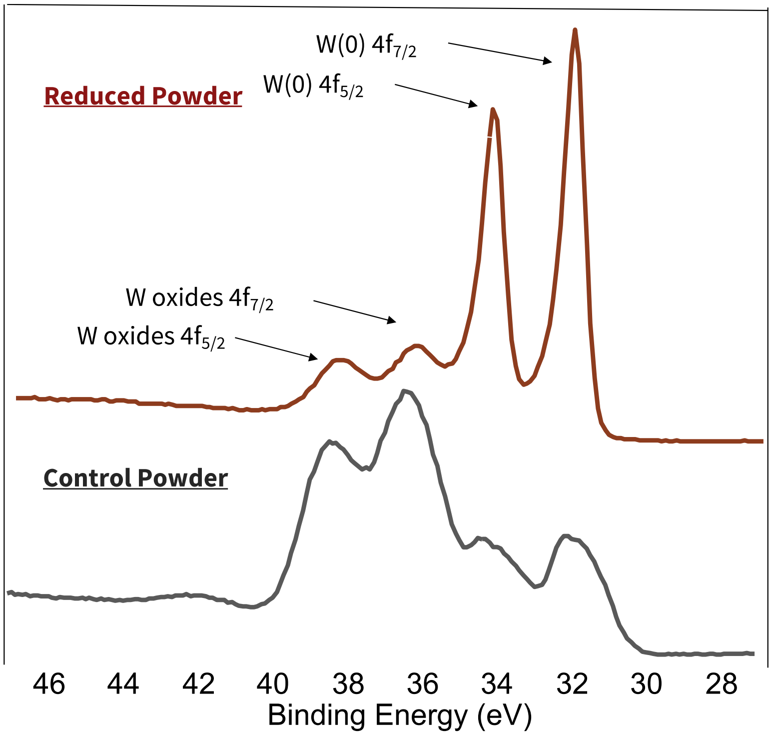

Figure 3.6. XPS measurement of control powder vs reduced oxygen powder.

Metallographic cross sections of control and reduced oxygen tungsten 3D prints were observed under SEM and show that reduced oxygen samples show less microcracking as compared with control samples. Specifically, as the thickness of walls increased from 250 um to 1 mm, crack density tends to increase with the control samples, but stays nearly crack free for the reduced oxygen samples. The results of this analysis can be seen in Fig. 3.7.

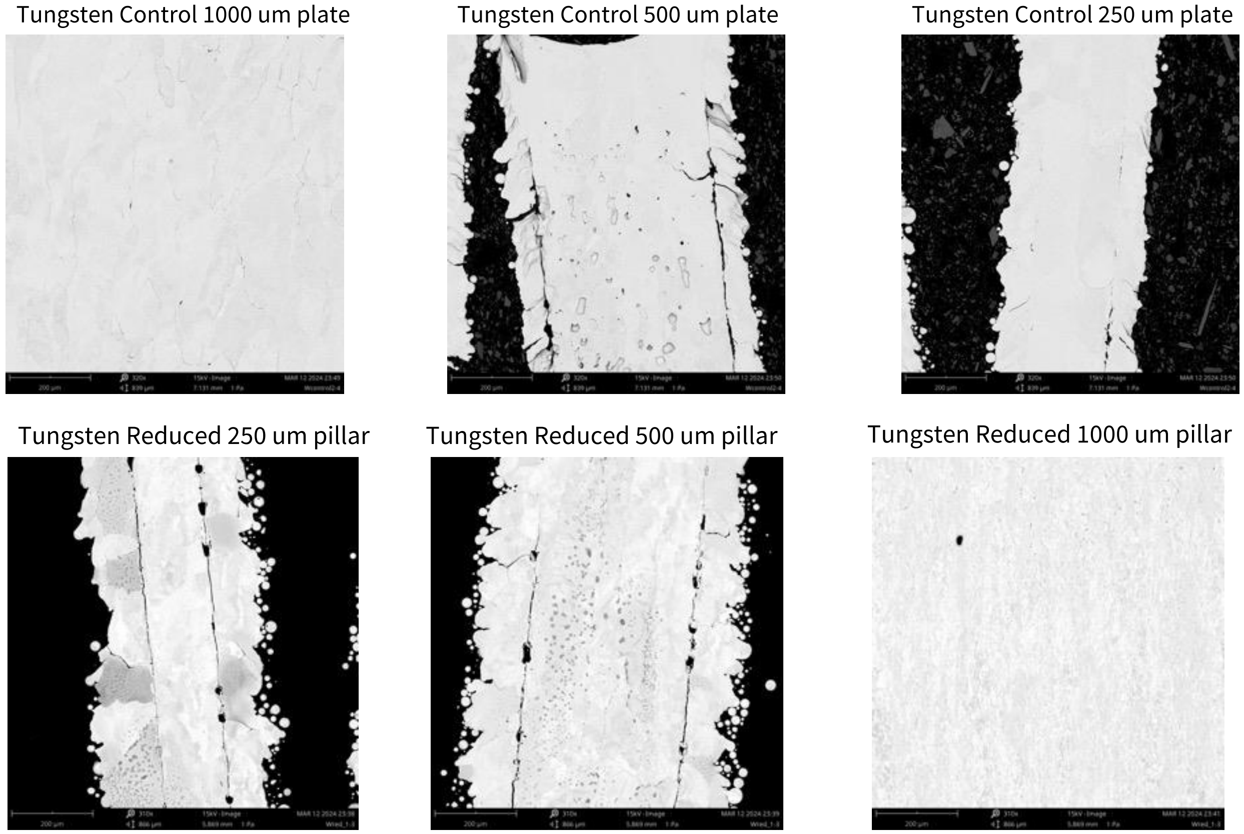
Tungsten Control 1000 um plate

Tungsten Control 500 um plate

Tungsten Control 250 um plate

Tungsten Reduced 250 um pillar

Tungsten Reduced 500 um pillar

Tungsten Reduced 1000 um pillar

Figure 3.7. 3D full builds of tungsten thin plates. Top: Control prints with nominal oxygen content. Bottom: Reduced oxygen samples, showing the absence (or marked reduction) of cracking.

While encouraging results are shown for reducing oxygen, and therefore crack density in elemental tungsten, more experiments are needed to determine a more robust relationship between oxide reduction and defect density in LPBF tungsten. Total time, temperature, and hydrogen concentration of reduction experiments are important parameters in understanding the roll of oxygen in defect formation in elemental tungsten printing.

4 **Printing Complex Ta-10W Geometries**

The main challenge in printing complex parts in LPBF resides in the ability to control distortions induced by residual stresses, which reduce the flexibility to print parts with low-angle overhangs making it necessary to include supporting structures, as well as diminishes the quality of the finished surfaces. For Ta-W alloys, the additional challenge of avoiding the appearance of microcracks and pores exists.

4.1 Experimental/modeling approaches

We performed standard parametric studies to determine printing parameters to print Ta-W parts. We first printed three sets of twenty-four small cuboids each for Ta, Ta-2.5W, and Ta-10W, respectively, using a zig-zag strategy with a 90° rotation under varying processing parameters. Two laser power (170 and 200W), two hatching spaces (0.05 and 0.1 mm), and five scan speeds (50, 100, 200, 400, and 800 m/s) conditions were used. Each cuboid size was 2 mm long, 2 mm wide, and 1 mm thick. Each set was printed on a 25.4-mm diameter Ta-substrate. The printing chamber was tightly sealed and maintained under an argon gas atmosphere with oxygen content below 100 ppm.

To devise novel printing strategies when the laser needs to hatch over fresh powder, the scenario that appears when printing overhangs, we explored a family of strategies that divided a slice to print into three areas: (a) a bulk area, composed of all the points at a distance away from the boundary of the slice, (b) downskin area, composed of all those points at a small-enough distance from the boundary of the slice, and (c) a bulk-to-downskin area transitioning between the two; see Fig. 4.1. As with the cubes, we performed a parametric study of laser scan speed, power, hatching distance and determined the range.

To do this, we first built custom made software that allowed us to program these strategies as G-code for the printer. All prints took place in the Trumpf 1000 machine at Stanford.

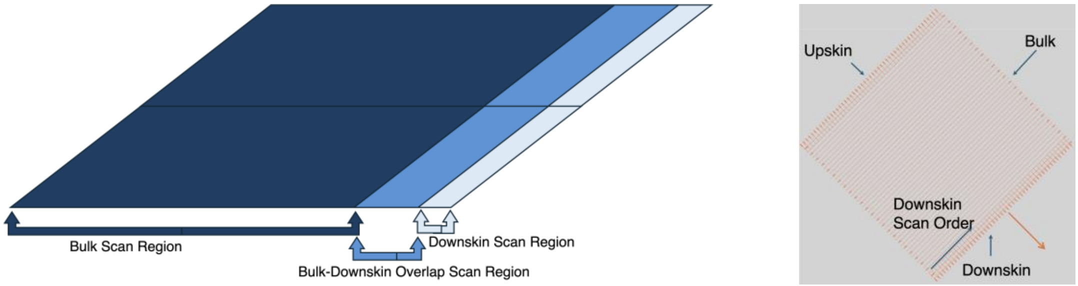

Figure 4.1. Printing strategy to build overhangs. Left: side view of the strategy for an inclined plane. Right: Top view of a slice.

Various microscopic techniques, including X-ray diffraction (XRD, PANalytical Empyrean), a commercial optical microscopy (OM), scanning electron microscopy (SEM, TFS APreo), energy dispersive X-ray spectroscopy (EDS, JEOL JSM-IT500HR), and electron backscatter diffraction (EBSD, TFS APreo), were employed to analyze defects and microstructures. The conditions for polishing and etching varied slightly depending on the purpose and are detailed in Table 4.2. Compression testing was performed using a universal testing machine (MTS Criterion Series 40).

At this point, we have not had the chance to look into the microstructure induced in the inclined planes.

Method	**Processing**
General OM, XRD	Polishing was performed using a 600-grit sandpaper.

General SEM, EDS	Polishing was performed using 600, 800, 1200, and 2000-grit sandpapers.
SEM to reveal microstructures	Polishing was performed using 600, 800, 1200, and 2000-grit sandpapers, followed by etching with a solution consisting of 50% sulfuric acid, 20-30% hydrofluoric acid, and 20-30% nitric acid.
EBSD	Polishing was performed using 600, 800, 1200, and 2000-grit sandpapers, followed by electro-polishing with a solution of 90% sulfuric acid and 10% hydrofluoric acid at 30V, 0.1A for 10 minutes at ambient temperature.

Table 4.2. Processing methods used for microscopic analysis

4.2 Results/Outcomes

Figures 4.2 (a), (b), and (c) show the top view images of Ta, Ta-2.5W, and Ta-10W small samples produced with various process parameters, respectively. The Ta and Ta-2.5W samples contained minimal defects across most process parameters, indicating a wide processing map. However, the printed Ta-10W samples demonstrated a narrower processing map compared to the Ta and Ta-2.5W samples.

Figures 4.3 (a) and (b) present cross-sectional views of Ta and Ta-10W samples, respectively, produced at a low energy density of 106 J/mm^3 (the process conditions of 170W laser power, 800 mm/s scan speed, and 0.1 mm hatching space). These images reveal unmelted powders and pores oriented perpendicular to the building direction. Meanwhile, Figure YYY shows that, when comparing the Ta, Ta-2.5W, and Ta-10W samples produced at a scan speed of 800 mm/s, Ta10W samples contain higher defect densities than Ta and Ta-2.5W samples even at the same energy densities.

Figure 4.4 shows a cross-sectional view of a Ta-10W sample produced with a laser power of 200W, hatching space of 0.05 mm, and scan speed of 50 mm/s (= 4000 J/mm^3). These cracks are observed to form long lines parallel to the build direction. Notably, the cracks grew linearly and then branch out near the surface, as indicated by the white arrow. The area marked with a black dashed square in Fig. ZZN (a) shows the initiation point of these cracks, and the magnified view in Fig. ZZN (b) reveals that micro-scale cracks formed along grain boundaries parallel to the build direction from the initial printing stages just above the substrate. In addition, pores are also observed along with the cracks, as shown in Fig. ZZN (a).

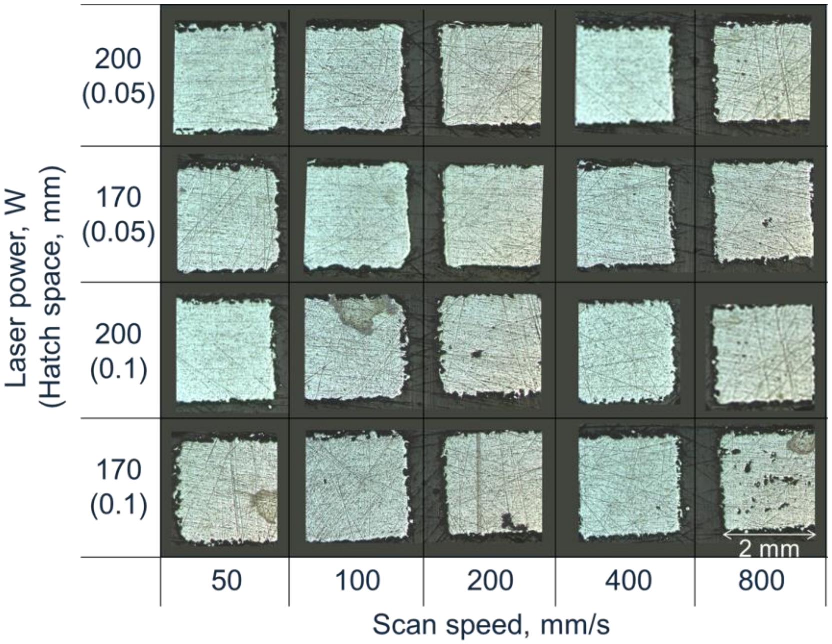
Laser power, W
(Hatch space, mm)
200 (0.05)
170 (0.05)
200 (0.1)
170 (0.1)
2 mm
50
100
200
400
800
Scan speed, mm/s

(a)

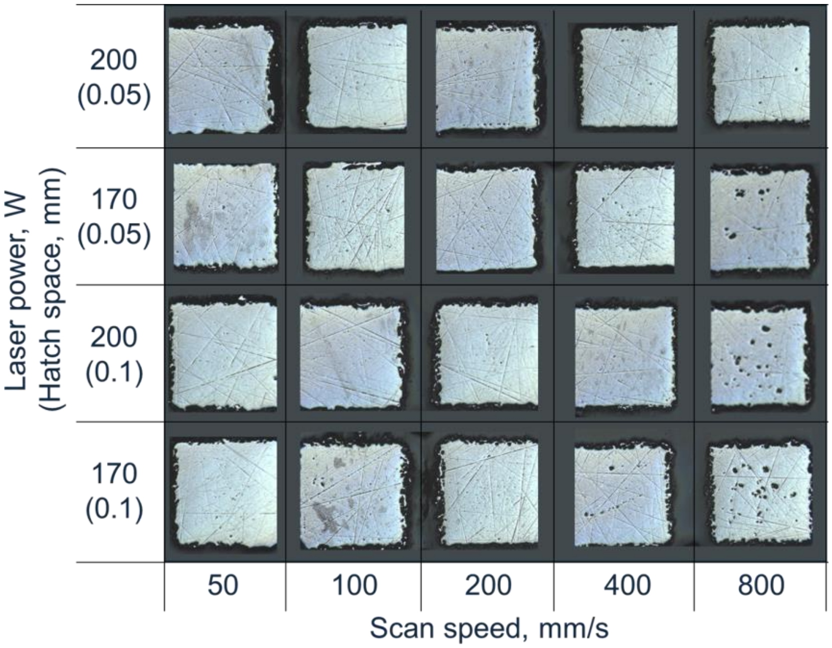
Laser power, W
(Hatch space, mm)
200 (0.05)
170 (0.05)
200 (0.1)
170 (0.1)
50
100
200
400
800
Scan speed, mm/s

(b)

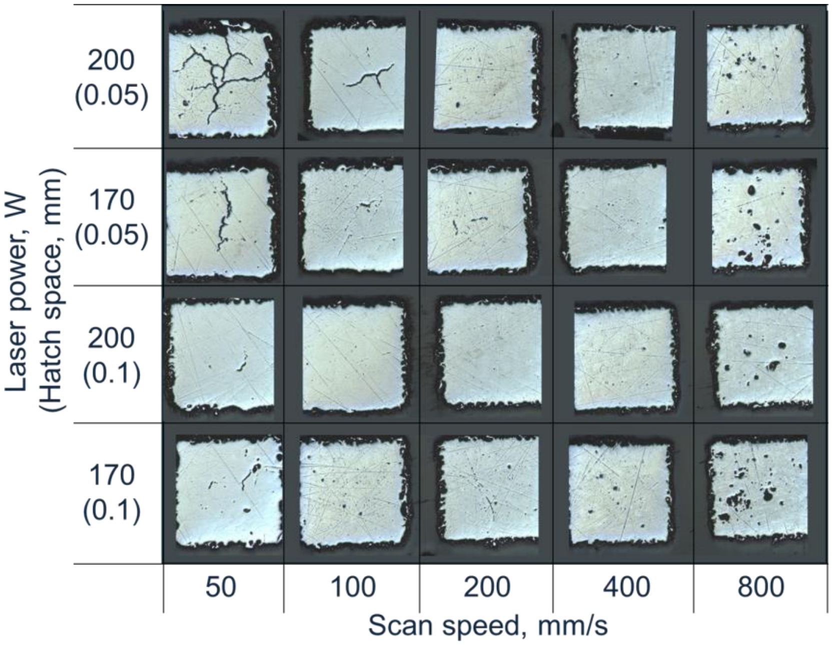

(c)

Figure 4.2. Top views for Ta, Ta-2.5W, Ta-10W samples fabricated under varying process parameters. A contour function was not used after printing.

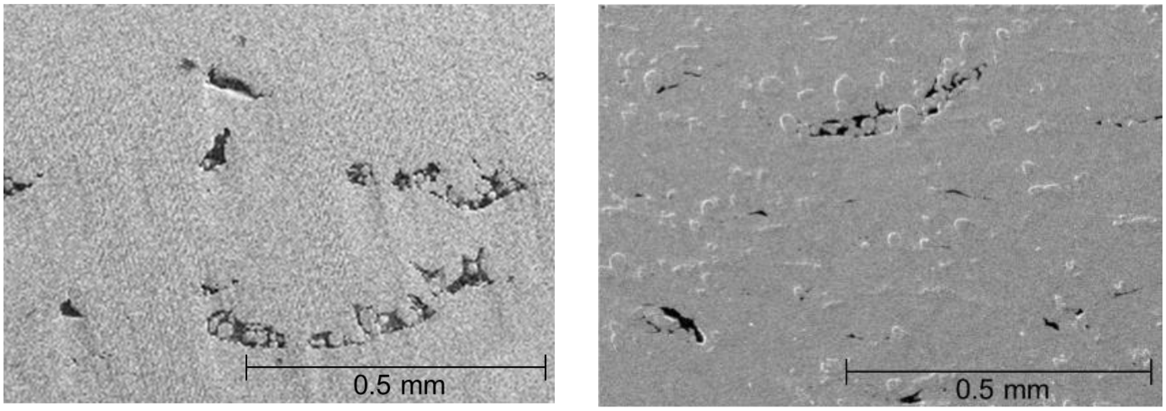

(a) (b)

Figure 4.3. Cross-section views of (a) Ta and (b) Ta-10W samples produced at an energy density of 106 J/mm^3 (the process conditions of 170W laser power, 800 mm/s scan speed, and 0.1 mm hatching space).

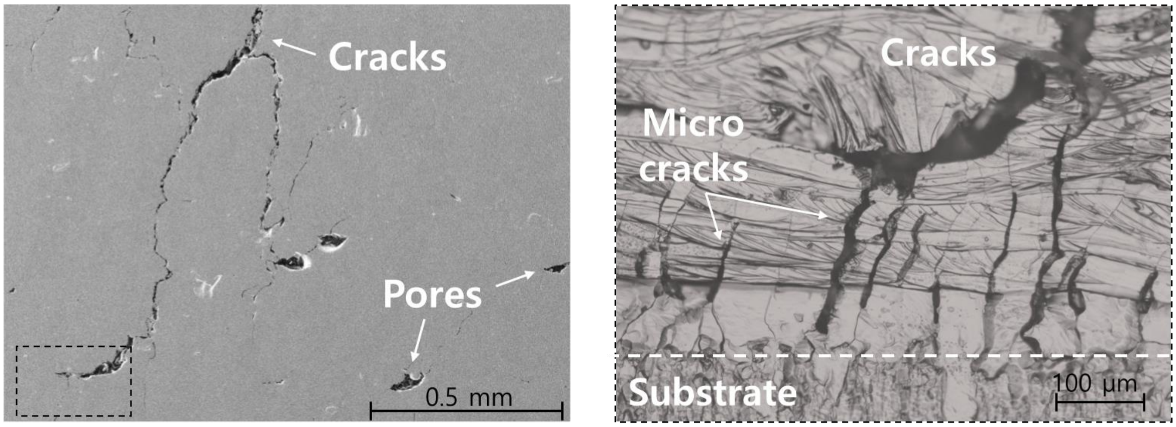

(a) (b)

Figure 4.4. (a) A cross-sectional view of a Ta-10W sample produced with a laser power of 200W, hatching space of 0.05 mm, and scan speed of 50 mm/s. (b) The magnified view of black dashed square in (a).

Figure 4.5 (a) shows a top-view image of pure Ta samples fabricated using 170W laser power, 400 mm/s scan speed, and 0.05 mm hatching space. Note that the surfaces were electro-polished and measured using SEM in a backscattered electron (BSE) mode. The "S" shaped grains, which are mirrored for neighboring tracks can be clearly observed between two scan track centerlines. Figure 4.5 (b) shows the microstructure of Ta-10W, which was created using the same processing parameters as the Ta sample above, exhibited a substantially refined microstructure in contrast to the Ta. Near the centerline, smaller equiaxed grains in the range from 2 to 10 µm, were observed. The track width of the Ta and Ta-10W was approximately 96 µm, corresponding to the hatching space (100 µm) used for printing.

Figure 4.6 presents the EBSD inverse-pole-figure (IPF) images for Ta and Ta-10W. The top-view image of Ta (Fig. 4.6 (a)) reveals track patterns and grain morphology that are almost identical to that observed in previous SEM results. A checkerboard pattern, with most grains oriented in the <111> direction (blue color) and a few in the <100> direction (red color), is clearly shown in Ta. A similar observation has been reported in [7]. In contrast, the EBSD top-view of Ta-10W (Fig. 4.6 (b)) shows much smaller grains, as observed in the SEM images. Although there is a slight increase in randomly oriented grains compared to pure Ta, most of the grains still predominantly align in the <111> direction. Figure 4.6 (c) shows an EBSD cross-sectional view of Ta, where strong columnar grains, predominantly oriented in the <111> direction along the build direction, are observed, again consistent with findings reported in [7]. In Figure 4.6 (d), Ta-10W also exhibits columnar grains along the build direction, but they are less pronounced compared to Ta. Additionally, equiaxed refined grains with more random textures are observed in Ta-10W. A IPF color key is presented in Figure 4.6 (e).

Figure 4.7 shows a melt-pool cross-section in Ta-10W where cell structures are observed that do not appear in Ta. In the melt pool, equiaxed cells are found at the center (a), elongated cells in the middle (b), and an absence of cells at the edges (c). This observation is a typical phenomenon in AM processes, which originate from the relationship between the temperature gradient and the solidification rate within the melt pool.

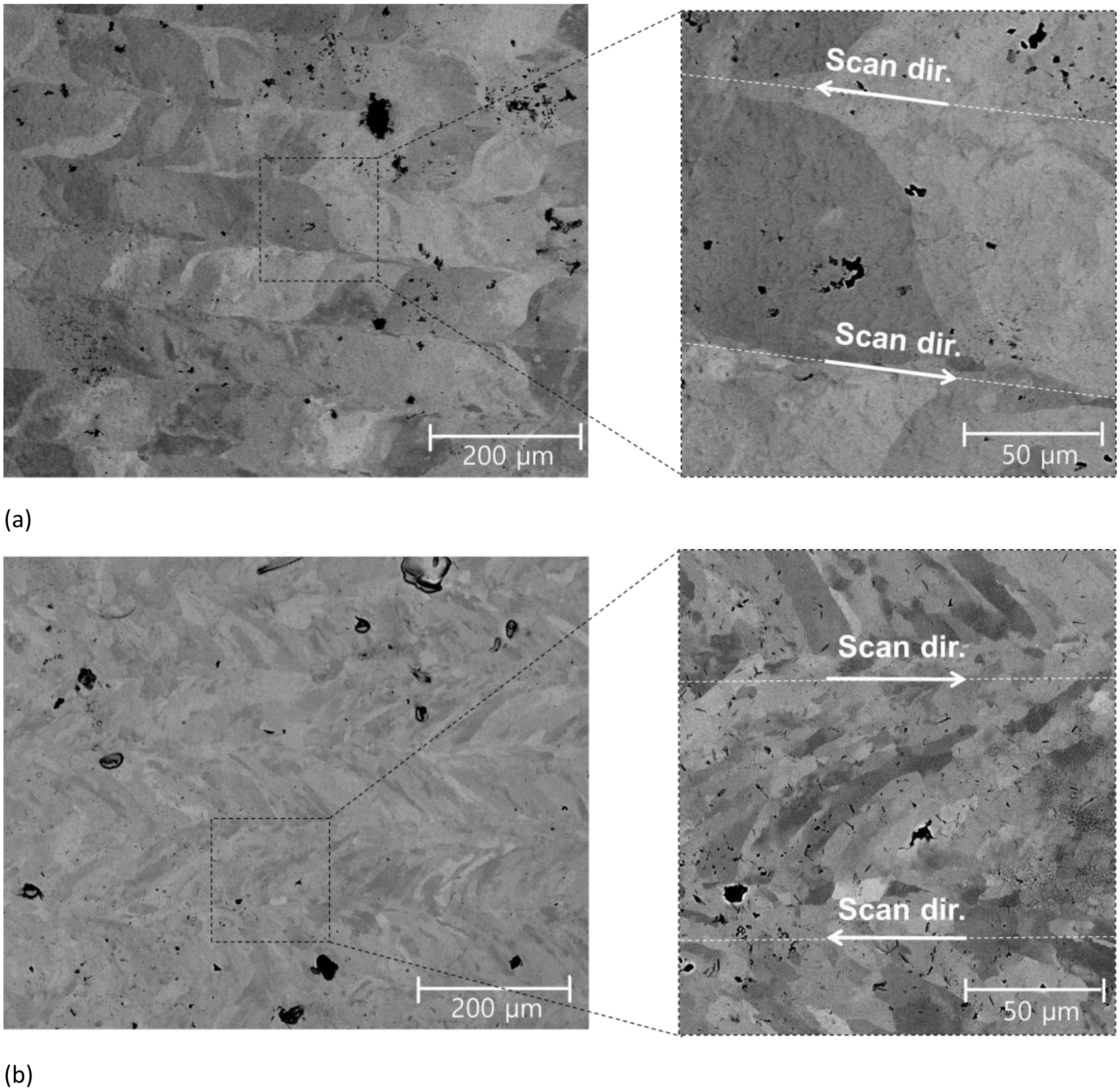

Figure 4.5. Top-view SEM-images of (a) pure Ta and (b) Ta-10W samples, respectively, fabricated under optimal process parameters.

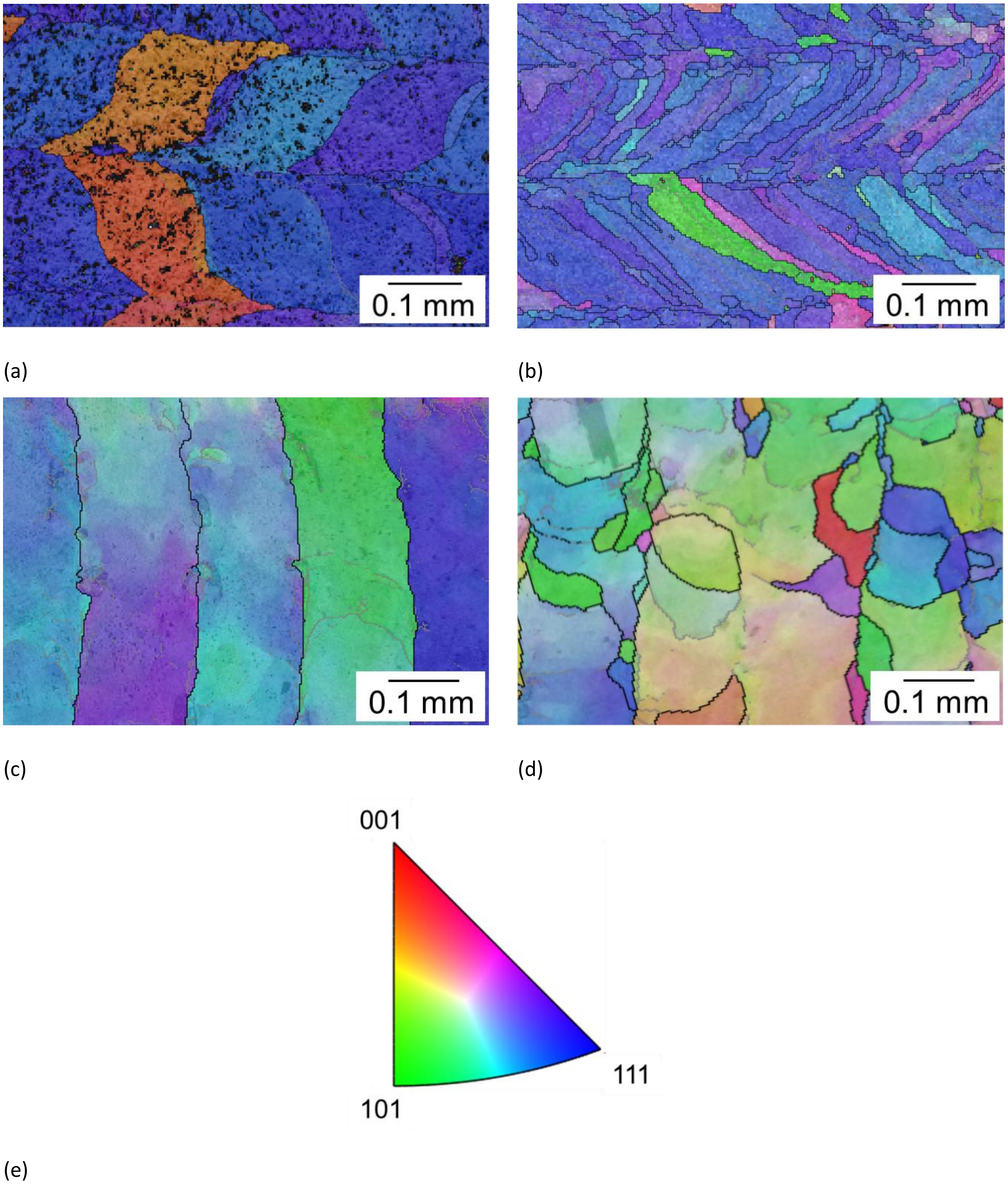

Figure 4.6. EBSD IPF maps: top views for (a) Ta and (b) Ta-10W, respectively, and cross-section views along the build direction for (c) Ta and (d) Ta-10W, respectively. (e) The IPF color key.

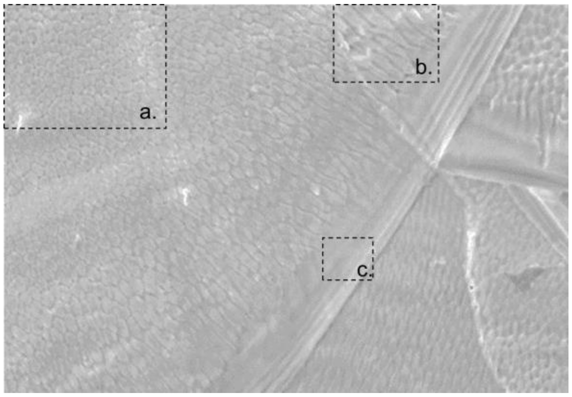

Figure 4.7. (a) Equiaxed cells at the center, (b) elongated cells in the middle, and (c) an absence of cells at the edges in a Ta-10W melt-pool.

The representative engineering stress-strain curves of pure Ta, Ta-2.5W, and Ta-10W are shown in Fig. 4.8. The mean compressive yield strengths of each sample, averaged over three measurements, were 505 ± 8 MPa, 691 ± 23 MPa, and 1081 ± 90 MPa, respectively, in the order of Ta, Ta-2.5W, and Ta-10W. Our Ta-10W samples exhibited a yield strength approximately 300 MPa higher than those reported for Ta-10W produced by EBM AM in previous studies. Notably, while pure Ta is known for its excellent ductility, the Ta-2.5W and -10W alloys also exhibited impressive compressive ductility, as they did not fracture until the machine stops (approximately at 90% strain).

Based on the analysis of Ta, Ta-2.5W, and Ta-10W alloys, we proceeded to print Ta-5W. The Ta-5W powder was prepared using the same powder mixing method, and the printing was performed using process parameters that fall between those used for Ta-2.5W and Ta-10W (170W laser power, 400 mm/s scanning speed, and 0.05 mm hatching space). Compression testing revealed that the yield strength of Ta-5W was 839 MPa, which fell between those of Ta-2.5W and Ta-10W, as expected. This result suggests that by using the process parameters identified within our process map, it is possible to fabricate up to Ta-10W alloys using in-situ alloying of LPBF, without needing pre-alloyed powders. However, when we attempted to print Ta-20W, defects were observed across most of the process map established for Ta-10W, indicating that further research is necessary to address these issues.

The development of strategies to print inclined planes with different overhang angles began with the key observation shown in Fig. 4.9. When printing the overhangs with the strategies discussed in Section 4.1, the length of the overhang turned out shorter than expected. This led to further exploration of the parameter space until the geometry was correctly reproduced. Examples of the type of overhangs that we have been able to print after the optimization are shown in Fig. 4.10.

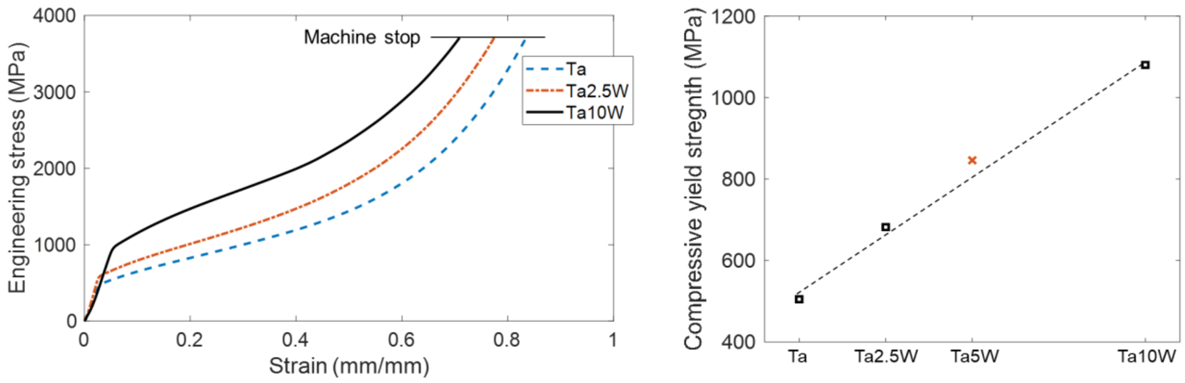

(a) (b)

Figure 4.8. (a) Engineering stress-strain curves for Ta, Ta-2.5W, and Ta-10W, respectively, obtained using compressive testing. (b) Compressive yield stresses of Ta-5W with Ta, Ta-2.5W, and Ta-10W results.

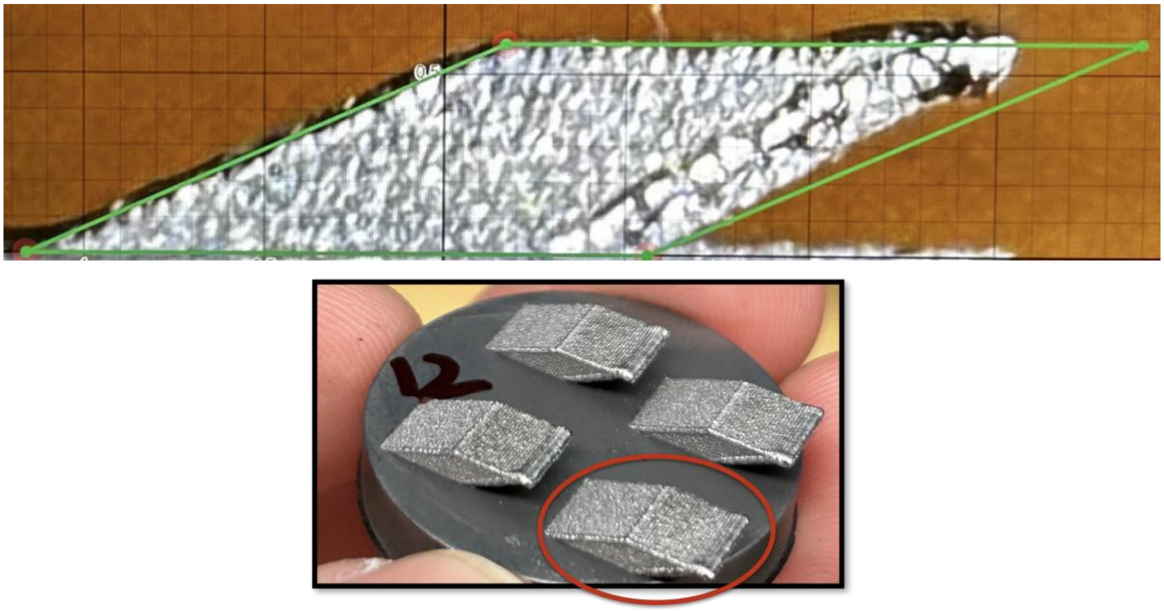

Figure 4.9. Printing inclined planes revealed that the resulting geometry differed from the expected one. The difference in cross sections grows with height, eventually leading to failure of the print. The part shown above is the one circled in red in the picture at the bottom.

As a result of this optimization, we built a curve indicating the optimal print parameters for each downskin angle, in Fig. 4.11. These curves were then used to adjust the printing parameters to print the geometries in Figs. 1.1 and 4.12.

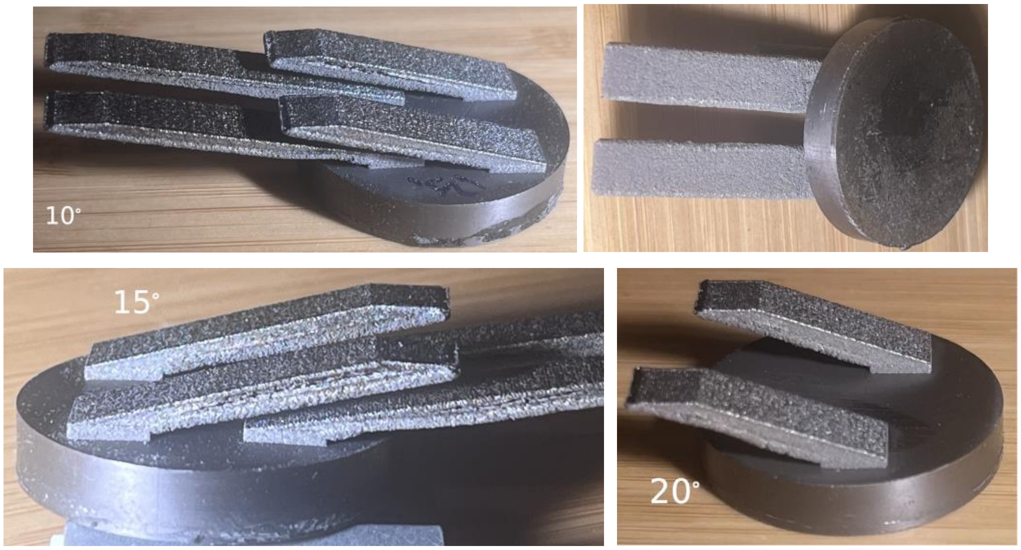

Figure 4.10. Inclined planes printed while testing several nearly optimal strategies. The top right also shows the bottom surface, or downskin, which is remarkably nice for a typical print. No supports were used in these prints.

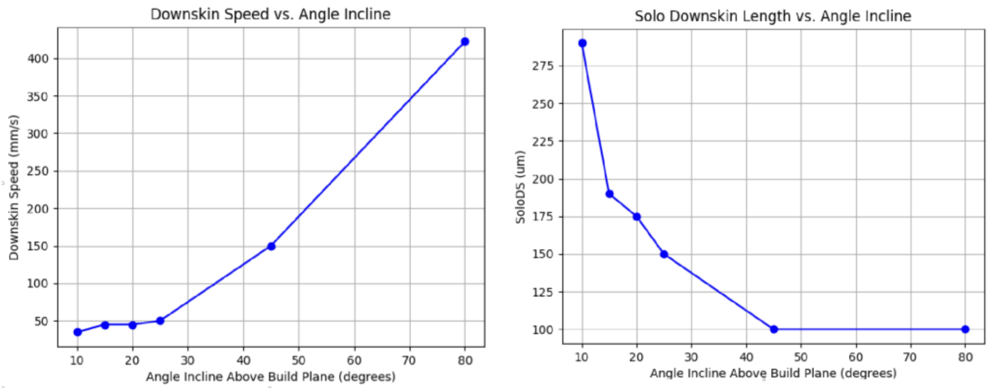

Figure 4.11. Printing parameters for the downskins as a function of the angle it forms with the horizontal. The power was kept constant at 150W. As a calibrated method, these curves need to be reproduced for each printer.

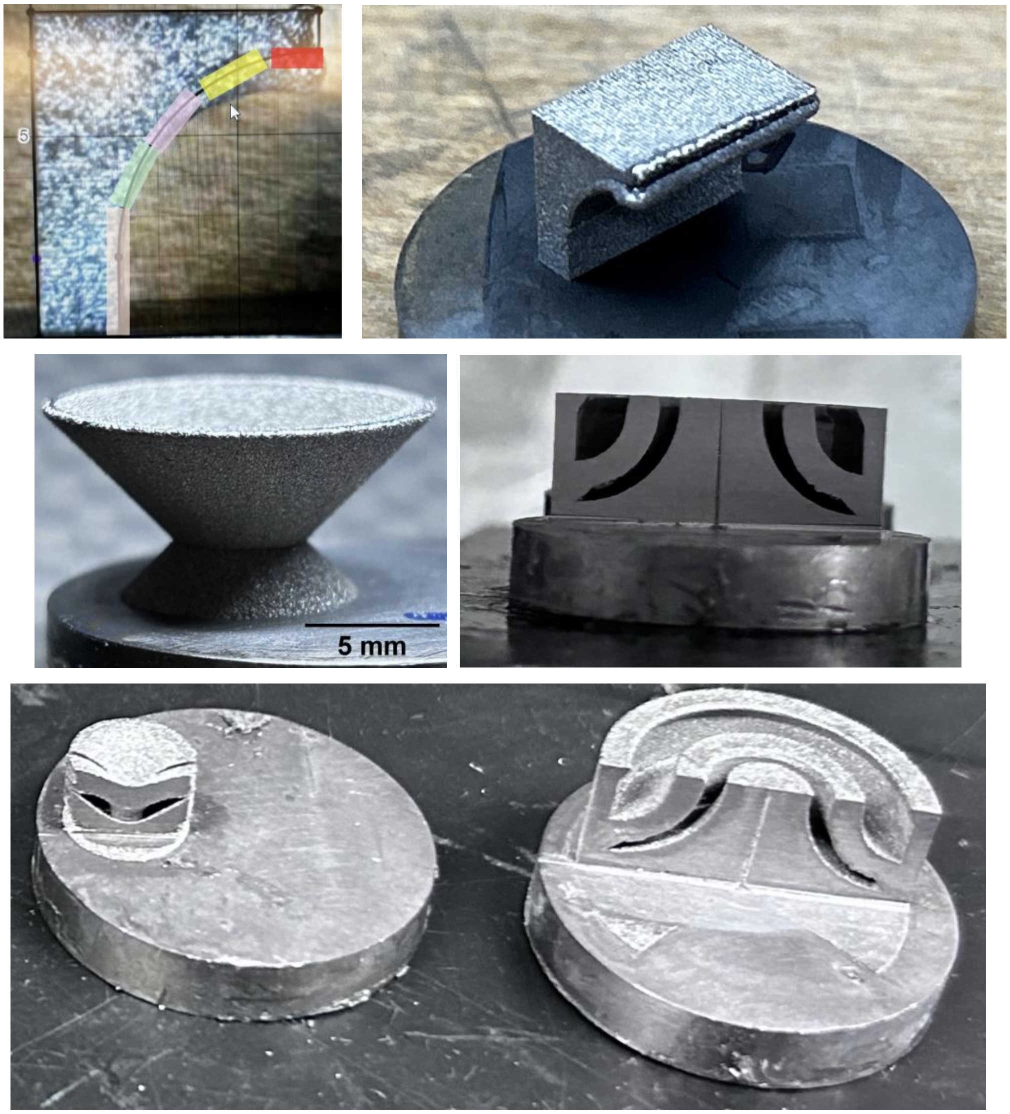

Figure 4.12. Additional printed complex geometries to those in Fig. 1.1. On top left, each color indicates a different set of parameters used to print the section of the surface.

6 Summary

In this project we have: (a) proposed, tested and validated strategies to print Ta-W alloys with no visible cracks or low crack density in the range of 0% to 10% W, (b) devised a novel strategy to print Ta-W alloys with overhangs avoiding supporting structures and with downskins of remarkable quality, which can be generalized to other alloys, and was well tested for Ta-10W, (c) designed and tested a method to perform in-situ alloying of Ta and W, which could also be applicable to other alloys, and (d) showed that reducing the oxide of W powder substantially diminishes the crack density in simple printed W parts.

These results have opened avenues for further exploration with important practical implications. First, the strategy to print arbitrary geometries with no supports should be extended to: (a) Generalize the applicability to other alloys, that is, learning general principles for how to translate the learning from one alloy to the next, (b) build a proper slicer that can facilitate the use of this knowledge on arbitrary geometries, and could be further enrich with other strategies that may arise for other complex geometric features, (c) learn how to control the quality of the surface finish in the downskin by better understanding the physics of the new process we created. Second, the printing of tungsten-rich Ta-W alloys has been barely explored, and while the results on oxygen-reduced tungsten powder are encouraging, we have only begun to understand the intricate interplay between oxygen and tungsten. Third, we ran out of time to perform a proper mechanical testing of printed parts and characterize the microstructure of the new way to print overhangs. This needs to be performed If the results are to be used.

7 References

[1] Veronica Livescu, Cameron M Knapp, George T Gray III, Ramon M Martinez, Benjamin M Morrow, and Bineh G Ndefru. Additively manufactured tantalum microstructures. *Materialia*, 1:15–24, September 2018.

[2] Igor L Shabalin. *Ultra-High Temperature Materials I*, volume 9789400775879 of *Carbon (Graphene/Graphite) and Refractory Metals*. Springer, University of Salford, Salford, United Kingdom, June 2014.

[3] Erik Lassner and Wolf-Dieter Schubert. *Tungsten*. Properties, Chemistry, Technology of the Element, Alloys, and Chemical Compounds. Springer Science & Business Media, December 2012.

[4] Barabash V. ITER SDC-IC Appendix A (2013) ITER D 222RLN v3.3-Material Data. pages 1–235, March 2013.

[5] Uvarova, I.V. Kinetics of tungsten teioxide reduction by dey and humidified hydrogen. Powder Metall Met Ceram 19, 587–590 (1980). https://doi.org/10.1007/BF00790543

[6] Seede, Raiyan, et al. "An ultra-high strength martensitic steel fabricated using selective laser melting additive manufacturing: Densification, microstructure, and mechanical properties." Acta Materialia 186 (2020): 199-214.